Journal of Materials Chemistry A

ROYAL SOCIETY OF CHEMISTRY

PAPER

View Article Online
View Journal | View Issue

Check for updates

Cite this: *J. Mater. Chem. A*, 2025, **13**, 8865

Free-standing graphene films decorated with lithiophilic particles as host electrodes for lithium plating/stripping in anode-less lithium metal batteries†

Mingliang Bai, Min Zhong, * Wenzhuo Shen, Jiali Zhang and Shouwu Guo *

Received 1st November 2024
Accepted 18th February 2025

DOI: 10.1039/d4ta07788a

rsc.li/materials-a

The host electrode is key to the lithium plating and stripping in anode-less lithium metal batteries. In this work, we fabricate a series of free-standing porous graphene films decorated with lithiophilic particles of AlN@Li_3N, MgF_2, Li_2CO_3, and the Mg–Li alloy foil, and systematically explore their electrochemical properties as lithium-host materials in anode-less lithium metal batteries. We characterize the structures and morphologies of the multifunctional graphene films before, after, and during lithium plating/stripping, to elaborate on the effects of different components in the film on the lithium plating/stripping. We demonstrate that the graphene sheets serve as an optimal host for lithium plating/stripping, the AlN@Li_3N, MgF_2, and Li_2CO_3 enable the formation of an inorganic LiF- and Li_3N-rich solid electrolyte interphase, and the Mg–Li alloy foil compensates for lithium loss during long-term cycling. The anode-less lithium metal batteries with the as-obtained graphene film as the host electrode, NCM811 as the cathode, and a carbonate-based electrolyte exhibit excellent electrochemical performance, with capacity retention reaching ~60% after 120 cycles at 1.93 mA cm^{-2}.

1. Introduction

Lithium-ion batteries (LIBs) have seen great developments during the last few decades, but the energy density of conventional LIBs lags behind the advancements in electric vehicles and other energy storage devices, which require an LIB energy density of > 350 W h kg^{-1} at the cell level.[1–3] As an anode, lithium metal shows a high specific capacity of ~3860 mA h g^{-1}, and a low redox potential of −3.04 V *vs.* the standard hydrogen electrode.[4] Thus, in recent years, the LIBs with lithium metal as the anode, termed lithium metal batteries (LMBs), have been considered as alternatives to traditional LIBs. However, there are still some drawbacks hindering the practical application of LMBs.[5] For instance, irregular lithium deposition, such as dendrite formation, causes quick battery failure.[6] The highly reactive lithium reacts with the electrolyte, causing unexpected consumption of both lithium and the electrolyte that leads to fast capacity fading.[7] Therefore, several protocols have been developed to overcome the obstacles, including host electrode designs,[8,9] the solid electrolyte interphase (SEI) modification,[10,11] and the electrolyte component innovation.[12,13]

Fairly speaking, typical LMBs reported so far show lower energy densities than LIBs because of the excessive use of lithium.[14] To further improve the energy density of LMBs, anode-less lithium metal batteries (AL-LMBs) have been proposed, which have a low N/P ratio (the ratio of anode to cathode in capacity) of ~0–1.[15,16] However, due to the lack of a suitable electrolyte and host electrode for lithium plating/stripping, AL-LMBs still suffer from rapid capacity loss. For example, an AL-LMB with a Cu‖NCM111 configuration shows a capacity retention of only 23% after the initial cycle.[17] To explore suitable host electrodes for lithium plating/stripping in AL-LMBs, a series of three-dimensional-network host materials have been studied, which in principle can disperse the local surficial current density, and thus can slow the growth of dendrites.[18] Among them, carbonaceous materials including carbon fibers,[19] carbon tubes,[20] carbon cloth,[21] and graphene[22] are often used, because of their availability and ease of chemical functionalization. However, carbonaceous hosts exhibit poor lithiophilicity in practice, and the morphology of the as-plated lithium is hard to control.[21] Hence, the lithiophilic particles are often introduced into carbonaceous hosts.[23] For example, a graphene skeleton decorated with ZnO nanosheets was prepared as a host electrode for lithium plating/stripping.[24] Additionally, lithiophilic designs can also incorporate interface regulation, such as using TiN-decorated carbon fibres as a host

Department of Electronic Engineering, School of Electronic Information and Electrical Engineering, Shanghai Jiao Tong University, Shanghai 200240, China. E-mail: zomi@sjtu.edu.cn; swguo@sjtu.edu.cn

† Electronic supplementary information (ESI) available: Additional XRM, SEM, and TEM images; additional nitrogen adsorption results; additional XPS spectra, particle size distribution, stress–strain, and ICP results; additional electrochemical results of half-cells and full-cells, *etc.* See DOI: https://doi.org/10.1039/d4ta07788a

electrode, which promotes the formation of a Li_3N-rich SEI.[25] Nevertheless, it is worth noting that as host electrodes for lithium plating/stripping, the coulombic efficiencies (CEs) of most carbonaceous materials including the graphene derivatives need to be improved once the N/P ratio approaches 0.[26]

In this work, we design and fabricate a series of free-standing thin films as host electrodes for lithium plating/stripping in AL-LMBs, using graphene sheets decorated with lithiophilic inorganic particles, and Mg–Li alloy foil. Predictably, the as-obtained graphene films should enhance the coulombic efficiency and reversibility of lithium plating/stripping owing to (1) the large porosity and uniform pore distribution, which facilitate compact lithium deposition; (2) the lithiophilic inorganic particles that guide lithium nucleation; (3) the Mg–Li alloy foil that compensates for the lithium loss; and (4) the *in situ* formation of LiF and Li_3N which stabilize the interface between the electrolyte and electrode. The compositions, structures, and morphologies of the thin graphene films before, after, and even during lithium plating/stripping are characterized complementarily with X-ray microscopy (XRM), X-ray photoelectron spectroscopy (XPS), scanning electron microscopy (SEM), and high-resolution transmission electron microscopy (HRTEM). The electrochemical properties of the as-obtained thin films as host electrodes for lithium plating/stripping are evaluated in both half-cells and full-cells using a commercial carbonate-based electrolyte. The underlying mechanisms are discussed systematically. As will be shown, using the as-fabricated free-standing thin graphene film as the host electrode, $LiNi_{0.8}Co_{0.1}Mn_{0.1}O_2$ (NCM811) as the cathode, the AL-LMB shows a capacity retention of ~60% after 120 cycles with an average CE of ~99.4% at an areal capacity of 3.86 mA h cm^{-2} and a current density of 1.93 mA h cm^{-2}.

2. Results and discussion

2.1. Preparation and characterization of the graphene films decorated with lithiophilic inorganic particles

The detailed preparation procedure for the free-standing graphene films decorated with and without inorganic (lithiophilic) particles, abbreviated as LAG and AG film, is summarized in the experimental part. The three dimensional (3D) morphology of the as-obtained LAG film is first characterized with X-ray microscopy (XRM) imaging followed by structure reconstruction. To achieve this, slices of the film are obtained through XRM imaging, as shown in Fig. S1.† Subsequently, the slices are reconstructed using software (*Dragonfly*), as shown in Fig. 1a and in the Movie in the ESI.†[27] Meanwhile, four grey-scale density levels are recognized: the high (>3 g cm^{-3}), medium (>2 g cm^{-3}), low (>1 g cm^{-3}), and zero density regions are assigned to AlN/MgF_2, Li_2CO_3, graphene sheets, and pores, respectively. Accordingly, four regions of interest (ROIs) are created based on grey-scale divisions. The distinct peak at ~0 grayscale corresponds to the pores with a contrast-to-noise ratio between the pores and graphene of ~2.1 (Fig. S2†), which is considered to represent good contrast.[28] As illustrated in Fig. 1b, the LAG film is filled with numerous micro-scale pores, which most probably originate from the interconnection of graphene sheets. The volumetric and areal ratios of pores are calculated through ROI analysis, yielding values of 52.5% and 49.5%, respectively (Fig. 1c and S3†). The average sizes of the as-decorated particles are a few micrometers in diameter, which are well consistent with the original particle sizes of AlN and MgF_2, respectively (Fig. S4†). Fig. 1d shows the cross-sectional SEM images, where the thin film is 34 μm thick, and contains well-distributed particles, consistent with the aforementioned XRM data and the energy dispersive spectrometer (EDS) mappings (Fig. S5†). In contrast, the AG film has an uneven porous structure, as shown in Fig. S6.† As depicted in Fig. 1e–g, the lattice fringes of the as-decorated inorganic particles on graphene sheets are observed through HRTEM, including 0.24, 0.23, and 0.21 nm corresponding to $d_{(101)}$ of AlN, $d_{(021)}$ of Li_2CO_3, and $d_{(210)}$ of MgF_2, respectively. Besides the as-loaded AlN and MgF_2, Li_2CO_3 forms most probably from the reaction of residual LiOH with CO_2 released during thermal treatment of graphene oxide (GO) and is the most common inorganic species in the SEI known to accommodate the huge volume fluctuations and accelerate the diffusion kinetics of Li^+.[29] Interestingly, $d_{(002)}$ of Li_3N is also detected (0.19 nm), which may result from the reaction between AlN and LiOH during the fabrication procedure ($AlN + 3LiOH \rightarrow 3Li_3N + Al(OH)_3$).

The structure of the LAG film was also characterized with X-ray powder diffraction (XRD). As shown in Fig. 2a, the weak and broadened XRD peaks of the aggregated graphene sheets,[30,31] AlN (PDF #70-2543), and MgF_2 (PDF #70-2742), can be detected. Besides, the peaks of Li_3N (PDF #78-2005) and Li_2CO_3 (PDF #83-1454) are also observed, demonstrating the *in situ* formation of Li_3N and Li_2CO_3. The thermogravimetric analysis (TGA) curves, Fig. 2b, show that ~20 wt% of Li_2CO_3 and ~7 wt% each of AlN@Li_3N and MgF_2 are loaded on the LAG film. Fig. 2c shows that the intensity ratio of the D (~1350 cm^{-1}) to G (~1600 cm^{-1}) bands (I_D/I_G) of the Raman spectrum of the LAG film is higher than that of raw GO, revealing that more defects accumulated on the graphene sheets in the LAG film, which on the other hand may provide more nucleation and storage sites for lithium metal.[22] Although the Raman signals from Li_2CO_3 at 712, 747, and 1459 cm^{-1} were difficult to distinguish, the ATR-IR spectra in Fig. S7† indicate the existence of Li_2CO_3 in the LAG film.[32]

To evaluate the chemical states of different components within LAG, XPS measurements were conducted. The survey XPS spectra, Fig. 2d, show that the atomic ratio of C to O increases after thermal reduction. The hyperfine C 1s and O 1s spectra (Fig. S8†) verify the reduction of GO and formation of Li_2CO_3. The N 1s peaks at 399.0 and 399.9 eV, Fig. 2e, demonstrate the existences of AlN and Li_3N. The formation of Li_3N occurs because the as-decorated AlN reacts with LiOH during the LAG preparation process, and the as-generated Li_3N seems to be attached to the surfaces of AlN particles. As depicted in Fig. 2f, the strong F 1s XPS peak at 685.3 eV reveals the successful decoration of MgF_2 particles on the graphene sheets. The Li 1s XPS peaks at 55.1 and 55.5 eV (Fig. S9†) further confirm the existence of both Li_3N and Li_2CO_3 in the LAG film. The atomic proportions estimated from hyperfine XPS spectra are summarized in Table S1.† These results undoubtedly prove the reduction of GO to graphene sheets, the successful loading of AlN and MgF_2 particles, and the *in situ* generation of Li_3N and Li_2CO_3 in the LAG film.

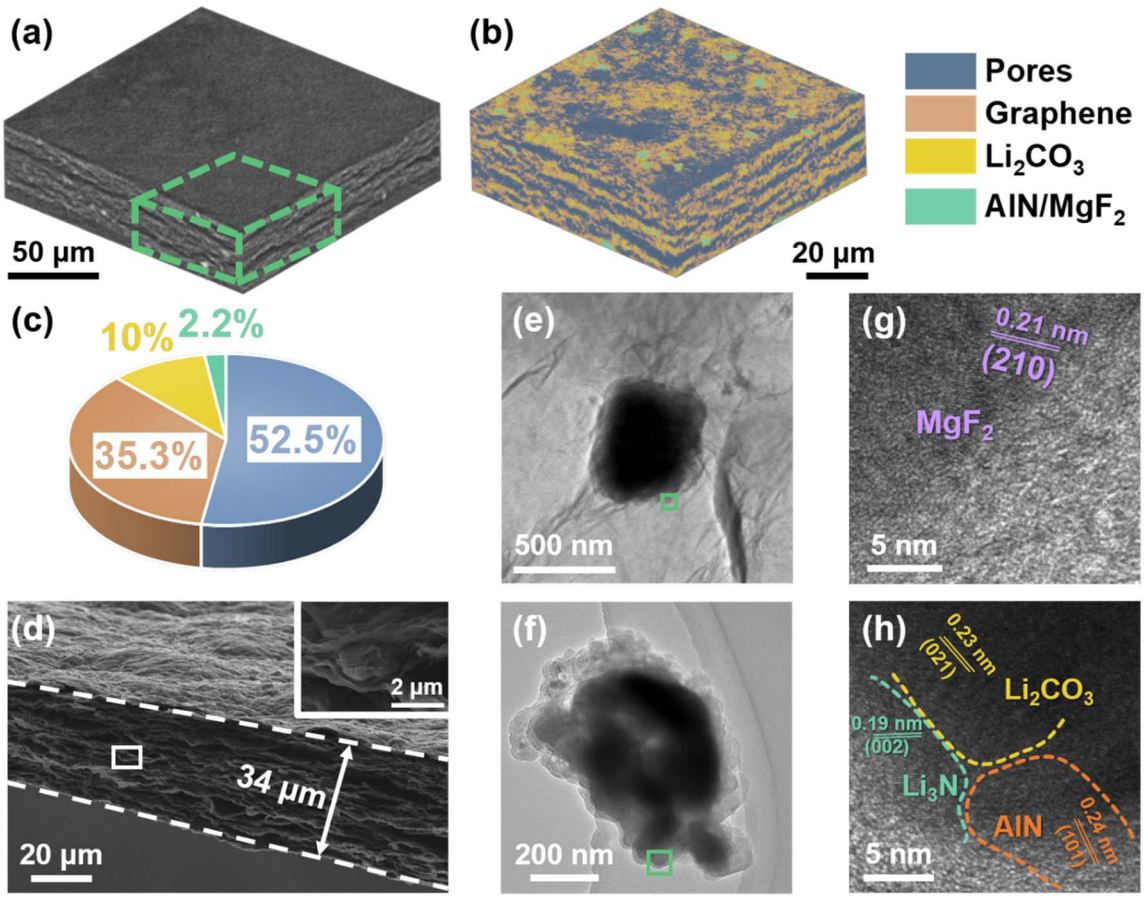

Fig. 1 (a) 3D XRM reconstructed images and (b) ROI distribution in the green box of LAG films. (c) Volumetric ratios of different components in LAG films. (d) Cross-sectional SEM image of a LAG film, with the inset showing a highly magnified image. (e and f) TEM images of the LAG film. (g and h) HRTEM images of the green sites in (e and f).

To understand the interactions among different components within the LAG film, the zeta potentials of GO, AlN, MgF_2, Li_2CO_3, LiF, and Li_3N are measured in water, 0.1 M LiOH aqueous solution (pH = 13), and dimethyl carbonate (DMC), respectively. As shown in Fig. 2g, GO sheets always show large negative potentials in water and 0.1 M LiOH aqueous solution, while AlN, MgF_2 and Li_2CO_3 show positive potentials in water and 0.1 M LiOH aqueous solution, demonstrating that the electrostatic interaction drives the decoration of AlN, MgF_2 and Li_2CO_3 onto the GO surface. For Li_3N, although it is affected by hydrolysis in water, it shows a weak negative potential (−3.65 mV) in 0.1 M LiOH aqueous solution (Fig. S10†). This means that the as-produced Li_3N may hardly exist alone, but can be attached to the positively charged surface of AlN particles. In DMC, as shown in Fig. 2h, GO sheets still exhibit a negative potential (−4.36 mV), while AlN and MgF_2 show positive potentials, meaning that even in DMC, a common solvent for electrolyte in LIBs, AlN and MgF_2 can remain stably decorated on the GO surface. Additionally, the zeta potentials of LiF, Li_3N, and Li_2CO_3 in DMC are also measured, showing values of −1.67, −1.02, and 1.27 mV, respectively. Obviously, LiF and Li_3N can still be attached to the graphene sheets through electrostatic interactions in DMC, which should be beneficial for the high quality SEI formation.[33,34]

Nitrogen isothermal adsorption measurements were performed, and the multi-point Brunauer–Emmett–Teller (MBET) and Barrett–Joyner–Halenda (BJH) methods are used for surface-area calculations and mesopore analysis. Notably, the LAG film has a larger MBET surface area and mesopore volume (Fig. S11†), along with rich porous features and a narrower mesopore distribution (Fig. 2i). These results are fully in agreement with the areal and volumetric analysis results obtained through 3D XRM reconstruction described above. The large surface area and pore volume provide the LAG film with adequate spaces for lithium plating. The narrow mesopore distribution, and the small pore size should help constrain lithium deposition to achieve reversible lithium plating/stripping. As shown in Fig. S12,† in contrast to the AG film, the LAG film shows higher mechanical strength, which may help accommodate the volumetric variation during lithium plating/stripping. As depicted in Fig. S13,† the LAG film also displays relatively lower contact angles with both water (~27°) and DMC (~7°), showing the better wettability.

2.2. Lithium plating and stripping performance of LAG films

To investigate lithium plating/stripping performances of LAG films, a series of coin half-cells were assembled using Cu foil, AG, and LAG films as host electrodes, lithium foil as the counter

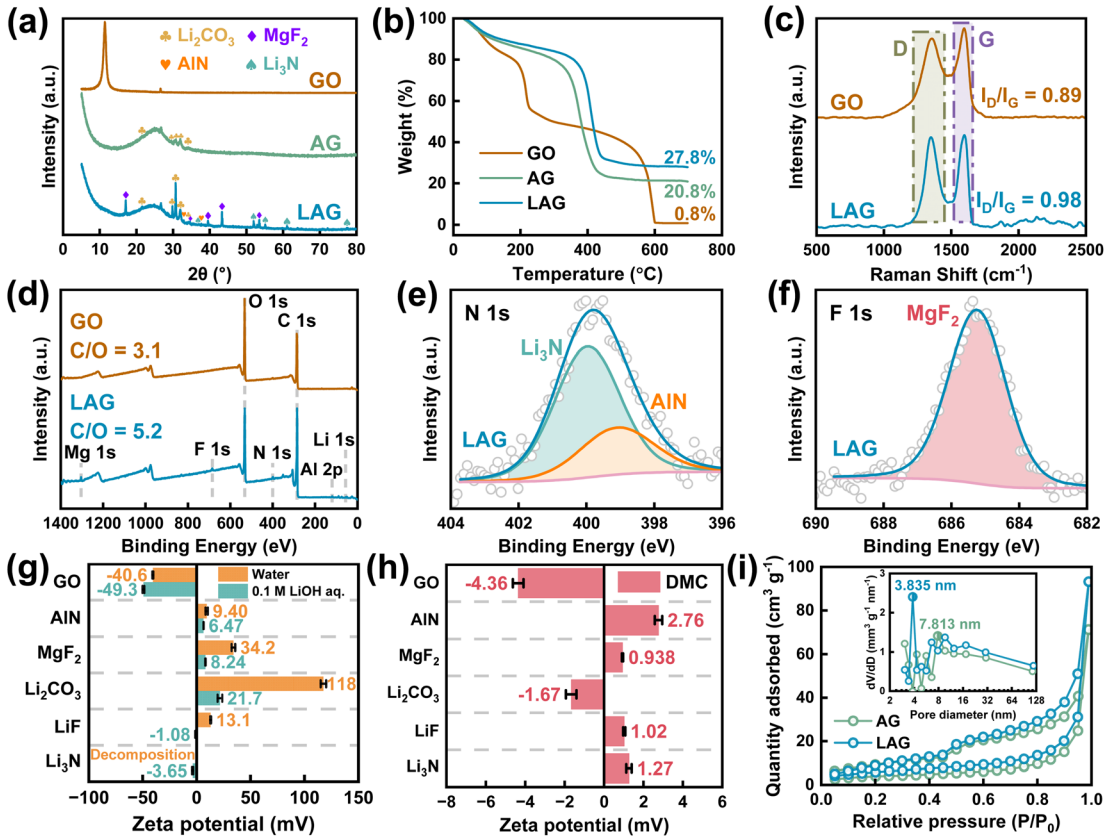

Fig. 2 (a) XRD patterns and (b) TGA curves of GO, AG, and LAG films. (c) Raman and (d) XPS survey spectra of GO and LAG films. (e and f) Deconvoluted XPS spectra of N 1s and F 1s of GO and LAG films, respectively. (g and h) Zeta potentials of GO, AlN, MgF_2, Li_2CO_3, LiF, and Li_3N in water, 0.1 M LiOH aqueous solution, and DMC, respectively. (i) Nitrogen isothermal adsorption curves of AG and LAG films, with the inset image showing mesopore distributions.

electrode, and a commercial carbonate-based electrolyte (1 M $LiPF_6$ in ethylene carbonate (EC)/diethyl carbonate (DEC)/dimethyl carbonate (DMC) (1/1/1, in vol) with 10% (in vol) fluoroethylene carbonate (FEC)). As shown in Fig. 3a, to observe the lithium nucleation process, a small current density is applied first. Clearly, Cu shows the highest nucleation overpotential (~61 mV) for lithium plating, because of its intrinsic lithiophobic surface.[35] AG shows a relatively low lithium nucleation overpotential of ~5.9 mV, because its porous multilayer structure induces lithium nucleation on graphene sheets. The LAG delivers the lowest nucleation overpotential of ~4.4 mV for lithium plating; this might be because it not only has a porous multilayer graphene structure, but also contains lithiophilic AlN@Li_3N and MgF_2 particles. Fig. S14† shows a potential *versus* ultimate areal capacity curve of LAG films. The lithium plating process on LAG films is steady, and an extraordinarily large areal capacity of 30 mA h cm^{-2} can be achieved, which is actually higher than that of most lithium hosts reported in the literature.[18] This result reveals the great lithium storage capacity of the LAG film, indicative of its large pore volume and surface area. Besides the nucleation overpotentials, coulombic efficiency (CE), and potential hysteresis, the potential difference between real plating and the ideally balanced deposition potential (0 V *vs.* Li^+/Li), are considered as the main factors affecting the lithium deposition.[36,37] The CEs of the aforementioned coin half-cells during long-term cycling at 1 mA cm^{-2} and 1 mA h cm^{-2} are shown in Fig. 3b, and the corresponding potential hysteresis values are calculated and displayed in Fig. 3c. The CE for lithium plating/stripping on Cu drops quickly after a few cycles accompanied by a fast increase in potential hysteresis, and the coin half-cell fails after <50 cycles, hinting at a possible short-circuit caused by adverse lithium dendrite formation, and electrolyte consumption through side-reactions.[38] The AG film delivers better lithium plating/stripping properties, including a stable potential hysteresis of ~30 mV, a high CE of ~96.7%, and a longer cycle life of over 250 cycles, because of its porous structure. In contrast, the LAG film exhibits the longest and most stable lithium plating/stripping cycling performance compared to Cu and AG. After 400 cycles, the average CE of LAG remains above ~98.6%, and the average potential hysteresis is as low as ~27 mV without an obvious increase (Fig. S15a and b†). As illustrated in Fig. S16a and b,† the galvanostatic charge–discharge (GCD) curves of LAG films show that the lithium plating/stripping potential platforms are almost overlapped during 400 cycles, demonstrating the high reversibility of lithium plating/stripping on LAG.

To further investigate the rate-capacity performance of LAG films during lithium plating/stripping, the coin half-cells were cycled at various capacities (Fig. 3d and e), and various current

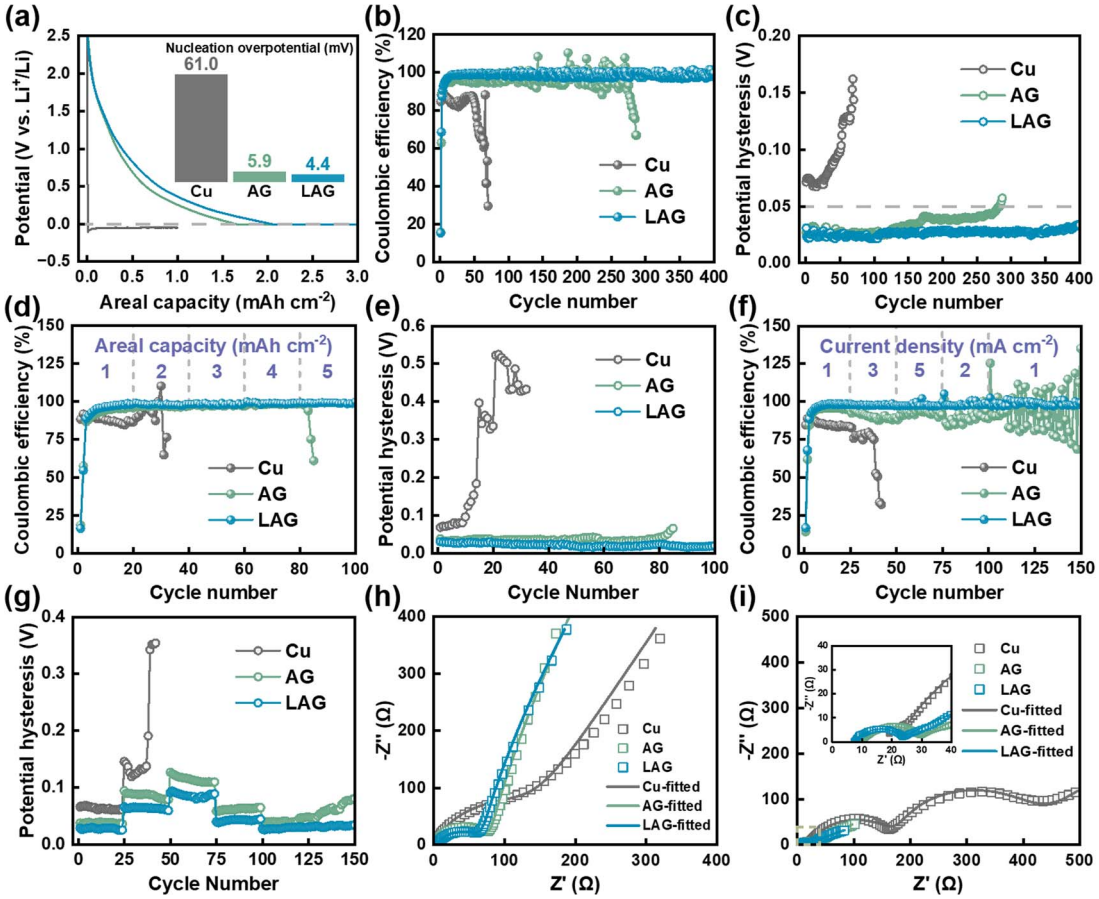

Fig. 3 (a) Lithium plating GCD curves at 0.1 mA cm^{-2} of Cu, AG, and LAG, with the inset image showing nucleation overpotentials. Lithium plating/stripping cycling performance of Cu, AG, and LAG at (b and c) 1 mA cm^{-2} and 1 mA h cm^{-2}, (d and e) 1 mA cm^{-2} and 1 to 5 mA h cm^{-2} for each 20 cycles, and (f and g) 1 mA h cm^{-2} and 1 to 5 mA cm^{-2} for each 25 cycles. (h and i) Nyquist plots before cycling and at SOC = 0% after the 50th cycle (1 mA cm^{-2}, 1 mA h cm^{-2}).

densities (Fig. 3f and g). At a moderate current density of 1 mA cm^{-2}, lithium can be plated/stripped reversibly on LAG with capacities ranging from 1 to 5 mA h cm^{-2}. The CE increases and the hysteresis decreases as the capacity increases revealing a good trade-off between the lithium plating/stripping rate and the capacity. As a matter of fact, the CE and hysteresis can reach ~98.9% and ~18.4 mV, respectively, even at a high areal capacity of 5 mA h cm^{-2} (Fig. S15c and d†), which are in full agreement with the GCD curves showing unique stationary plating/stripping platforms (Fig. S16c and d†). In contrast, the capacity of Cu is below 3 mA h cm^{-2}, and its hysteresis increases quickly to over 500 mV. At a capacity of 1 mA h cm^{-2}, LAG shows excellent stability for lithium plating/stripping cycles at varied current densities, with the CE remaining at ~97.6% at a current density of 5 mA cm^{-2} (Fig. S15e and f†). It is known that electrochemical polarization increases as the current density increases, and the hysteresis ascends gradually with increasing current density.[39] However, the rate of increase in hysteresis is for LAG is much slower than those of AG and Cu. The GCD curves of LAG at different current densities remain consistent, while AG shows anamorphic GCD curves with highly fluctuating CEs and a large increase in hysteresis (Fig. S16e and f†).

The Nyquist plots are acquired and fitted *via* the equivalent circuit in Fig. S17.† As shown in Fig. 3h and i, the LAG film exhibits the lowest Li^+ transport resistances across the SEI and charge transfer process resistances before cycling (R_{CT} of 65.9 Ω), and at SOC = 0% after the 50th cycle (R_{SEI} of 10.0 Ω and R_{CT} of 5.05 Ω, Table S2†), suggesting the unique interfacial properties of the LAG film, likely due to the decoration with AlN@Li_3N, and MgF_2 particles. The long cycling stability, highly stable CEs, and strong rate-capacity efficiency at large capacity and high current density for lithium plating/stripping, combined with the unique porous structure and lithiophilic characteristics make LAG a competitive host material for lithium plating/stripping.

2.3. Performances of LAG films as the host electrode in AL-LMBs

Considering the excellent lithium plating/stripping performances demonstrated in coin hall-cells above, a series of full-cells with NCM811 as the cathode and LAG as the host electrode for lithium plating/stripping were assembled, and their electrochemical properties were compared. As shown in Fig. 4a, the AL-LMB with LAG as the host, denoted as the LAG‖NCM811

cell, shows a large areal capacity of ~3.9 mA h cm^{-2}, using a carbonate-based electrolyte containing FEC; however the capacity fades to <2 mA h cm^{-2} after 30 cycles, indicating the possible lithium loss. To compensate for the lithium loss and suppress its effect on the full-cell cycling life, the LAG films are rolled iso-thickly with commercial air-stable Mg–Li alloy foil, LA103Z (consisting of ~10 wt% Li, ~3 wt% Al, ~3 wt% Zn, and ~84 wt% Mg, Table S3†); the films are named LAG/LA103Z films, with the thickness maintained at ~70 μm. Thus that, as illustrated in Fig. 4b, the The LAG/LA103Z||NCM811 cell shows a much slower capacity decay rate, achieving a higher capacity retention of ~60% after 120 cycles, and a high CE of ~99.4%. These results suggest, on the other hand, that the LA103Z foil does compensate for the lithium loss, affording the LAG/LA103Z||NCM811 with more stable charge/discharge plateaus compared to the LAG||NCM811 cell during continuous cycles (Fig. 4c and d). The Nyquist plots of full-cells are also measured and fitted *via* the aforementioned equivalent circuit. In Fig. 4e and f, the initial R_{SEI} and R_{CT} of the LAG/LA103Z||NCM811 cell are ~10.5 and ~13.1 Ω, and further decrease to ~7.8 and ~10.9 Ω at SOC = 0% after the 30th cycle (Table S4†); these values are much lower than those observed for the LAG||NCM811 cell as-studied. This shows the improved interfacial properties of the as-designed integrated bilayer film structure. For comparison, the LA103Z||NCM811 cell was also assembled but it showed a continuous and rapid capacity decline within <10 cycles, caused by uncontrollable interfacial side-reaction of alloy anodes (Fig. S18†).

Recently, to improve the electrochemical properties of AL-LMBs, electrolytes with high concentration[40] or high entropy[41] have been utilized. For examples, an AL-LMB using a Cu/polymer/Al composite as the host electrode, and a high concentration electrolyte consisting of 5 M LiFSI and 0.1 M $LiPF_6$ in FEC/DMC/tetrafluoroethyl-tetrafluoropropyl ether (TTE) (1/2/2, in volume) delivered a capacity retention of ~50% after 100 cycles, at a capacity of 1.8 mA h cm^{-2} and a current density of 0.9 mA cm^{-2}.[42] In contrast, as aforementioned, a commercial carbonate electrolyte (1 M $LiPF_6$ in EC/DEC/DMC (1/1/1, in volume) with 10 vol% FEC) is used in the LAG/LA103Z||NCM811 cell in our work, but the cells still exhibit competitive electrochemical performance, including higher areal capacity, longer cycling stability, and better rate capability. And the comparison details are summarized in Fig. 4g and Table S5.† To examine the effects of the electrolyte on the

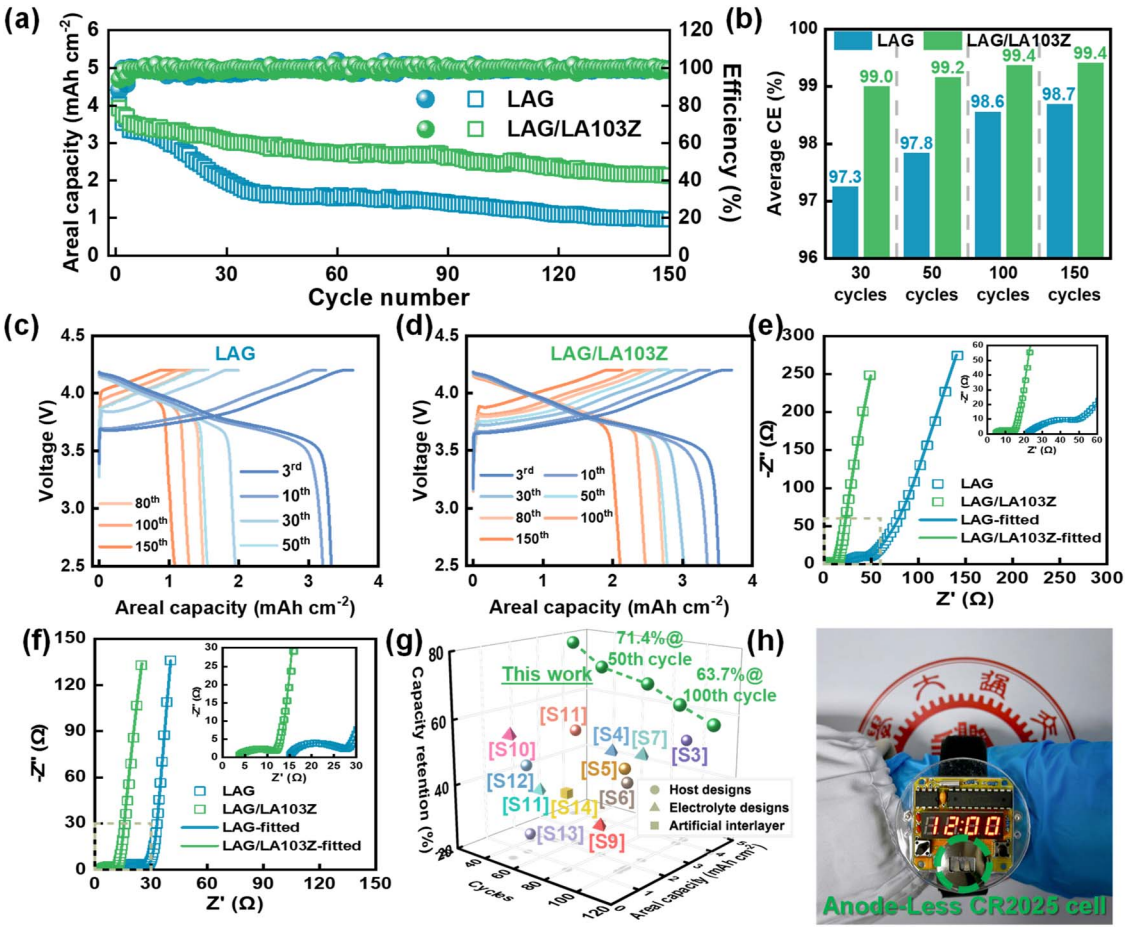

Fig. 4 (a) Charge/discharge cycling performances, (b) average CEs, and (c and d) GCD curves of LAG||NCM811 and LAG/LA103Z||NCM811 cells at 0.5C||0.5C, respectively. (e and f) Nyquist plots of LAG||NCM811 and LAG/LA103Z||NCM811 cells before cycling and at SOC = 0% after the 30th cycle. (g) Comparison of the electrochemical performance of the as-assembled LAG/LA103Z||NCM811 cell with AL-LMBs reported in the literature. (h) Digital photograph of the anode-less CR2025 cell powering an electronic watch (rated at 0.1 W and 3 V).

electrochemical properties of AL-LMBs with the LAG/LA103Z host electrode, LAG/LA103Z||NCM811 cells were also assembled using a carbonate electrolyte without FEC, and an ether electrolyte (1 M LiTFSI in 1,2-dimethoxyethane (DME)/1,3-dioxolane (DOL) (1/1, in volume) with 1 wt% $LiNO_3$), as shown in Fig. S19.† The cell using carbonate electrolyte without FEC shows a lower capacity retention of ~45% after 100 cycles, likely due to the instability of the carbonate electrolyte in the absence of FEC during lithium plating/stripping cycling.[43,44] The cell using ether electrolyte also exhibits a lower capacity retention of ~50% after 120 cycles due to the inherent poor electrochemical stability of ether electrolyte under high voltage.[45] In addition, to demonstrate its possible practical application, an electronic watch (rated at 0.1 W and 3 V) is successfully powered with the as-assembled LAG/LA103Z||NCM811cell (Fig. 4h).

2.4. Characterization of LAG during lithium plating/stripping

To gain insight into the evolution of the as-designed host electrode in AL-LMBs, the morphology variations of LAG films adhered to LA103Z during cycling are characterized using SEM. As depicted in Fig. 5a–c, after 30 cycles of lithium plating/stripping, the surfaces of LAG films remain intact, illustrating the excellent structural stability of LAG against volumetric fluctuations during lithium plating/stripping. This can partially explain the excellent cycling stability of the AL-LMBs. Furthermore, even at SOC = 100%, no surface-deposited lithium metal is observed, demonstrating that lithium plating/stripping happens within the pores of the LAG film. In contrast, during the same lithium plating/stripping process, the surface of Cu is destroyed severely, and irregular lithium dendrites could be detected at SOC = 100% (Fig. S20†). To identify the exact sites of lithium plating, the cross-sectional SEM images of LAG at SOC = 100% are acquired. As shown in Fig. 5d, the thickness of the LAG film at SOC = 100% is about 15.1 μm, indicating that the compact deposited lithium is homogeneously distributed between graphene sheets. This may be due to the 3D network motif of LAG, which suppresses the large volumetric changes during lithium plating/stripping. The EDS mappings of hetero-elements after lithium plating/stripping are also acquired. As shown in Fig. 5e–h, elements including Al, Mg, N, and F are distributed over the LAG, demonstrating that the AlN@Li_3N, and MgF_2 particles remain tightly anchored to the graphene sheets during cycling. This is understandable considering that these lithiophilic particles, such as AlN@Li_3N and MgF_2@LiF, guide lithium nucleation and deposition on their surfaces. Moreover, ICP-OES results directly illustrate the lithium compensation effect of LA103Z foil during cycling, which leads to much enhanced capacity retention of AL-LMBs (Fig. S21†). In addition, LA103Z foil in the LA103Z||NCM811 cell suffers from interfacial side-reactions to a great extent, irreversible lithium plating and stripping and huge and erratic de-alloying reactions, finally leading to uncontrollable structural degeneration (Fig. S22†).

It has been reported that the inorganic SEI components are the key factors affecting reversible plating/stripping, with LiF and Li_3N recognized as favorable inorganic components in the SEI.[46,47] To elucidate the composition of the SEI formed on LAG, TEM and XPS data are collected after lithium plating/stripping. As illustrated in Fig. 6a, TEM images show that nanoparticles are distributed uniformly on graphene sheets. The HRTEM images of these nanoparticles, Fig. 6b–d, demonstrate the lattice parameters of 0.20 and 0.14 nm corresponding to the $d_{(200)}$ and $d_{(220)}$ of LiF, 0.19 and 0.25 nm matching the $d_{(002)}$ and $d_{(110)}$ of Li_3N, and 0.21 nm consistent with $d_{(220)}$ of Li_2CO_3.[48,49] The loaded AlN particles are still observed on graphene sheets

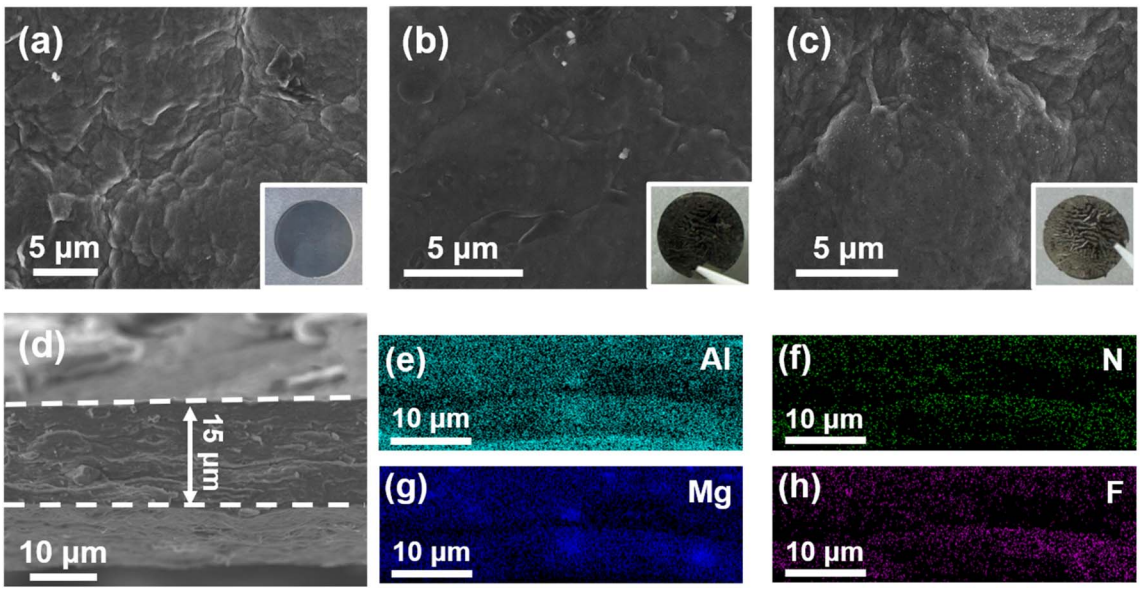

Fig. 5 SEM images of LAG films (a) before cycling and after the 30th cycle at (b) SOC = 0% and (c) SOC = 100%, with the inset showing the optical images of the corresponding electrodes. (d) Cross-sectional SEM image and (e–h) EDS mapping results of the LAG film at SOC = 100% after the 30th cycle.

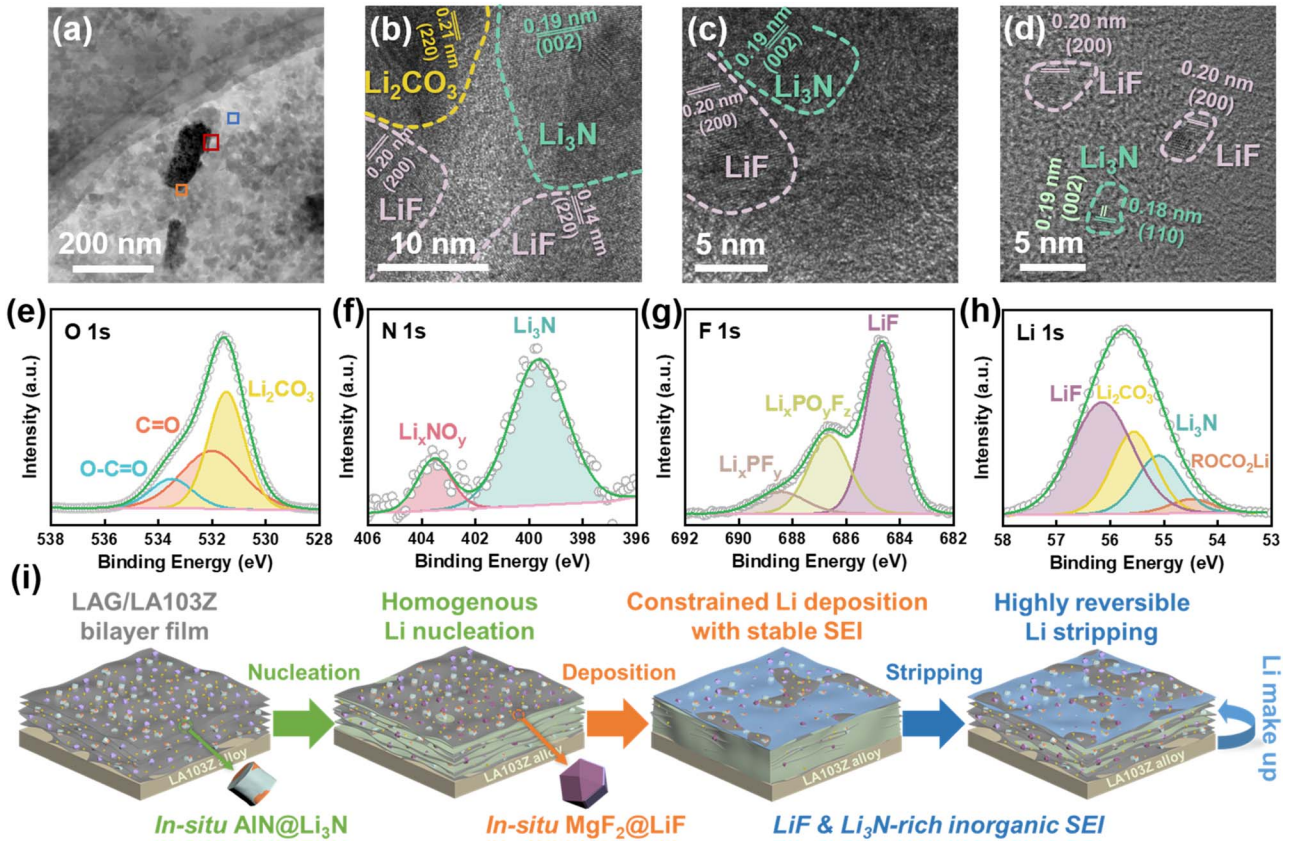

Fig. 6 (a) TEM images of LAG after cycling. (b–d) HRTEM images of the orange, red, and blue sites marked in (a). (e–h) O 1s, N 1s, F 1s, and Li 1s XPS peaks of the SEI formed on LAG. (i) Schematic illustrations of the morphological and interfacial evolutions of the LAG film.

(Fig. S23†). However, no lattice *d*-spacings of MgF_2 particles are detected; this might be because the as-decorated MgF_2 particles have been converted to LiF during lithium plating/stripping.

To quantitatively analyse the chemical compositions of the SEI formed on LAG, XPS measurements were conducted. The O 1s spectrum is deconvoluted, with hyperfine peaks at 532 and 533.5 eV corresponding to C═O and O–C═O, respectively (Fig. 6e). These species are mainly attributed to the decomposition of carbonate electrolyte to $ROCO_2$–Li species as dominant organic SEI components. And Li_2CO_3 (531.5 eV) is an essential inorganic SEI component. Thus, the SEI contains more inorganic but fewer organic species, as also confirmed by the C 1s spectrum (Fig. S24†). Fig. 6f shows the N 1s spectrum of the SEI. Clearly, a peak at 399.8 eV is detected due might to the *in situ* formation of Li_3N from the loaded AlN during lithium plating/stripping. Fig. 6g depicts the F 1s spectrum, where the peaks at 688.5 and 686.8 eV are attributed to Li_xPF_y and $Li_xPO_yF_z$, originating from the decomposition of $LiPF_6$. The lower content of these species suggests that the SEI may protect $LiPF_6$ from further side-reactions.[50,51] The peak at 684.7 eV corresponds to LiF, suggesting the formation of a LiF-rich SEI on LAG. From Li 1s peaks shown in Fig. 6h, it can be deduced that considerable contents of LiF (56.2 eV) and Li_3N (55.1 eV) are obtained. The calculated atomic proportions from the XPS spectra of the SEI are summarized in Table S6.† Specifically, the results show that the pre-loaded AlN and MgF_2 particles can enhance the formation of a LiF- and Li_3N-enriched SEI on the LAG host electrode surface. Additionally, the as-formed LiF and Li_3N-rich inorganic SEI should facilitate Li^+ transport, weaken the solvation coordination of solvated Li^+, and reduce interfacial resistance.[33,34,47]

Based on the aforementioned analysis, the morphological and interfacial evolutions of the LAG film facing the electrolyte during lithium plating/stripping cycling are schematically illustrated in Fig. 6i. Homogenous nucleation occurs on the LAG film, induced by lithiophilic *in situ* AlN@Li_3N and MgF_2@LiF, which guide lithium deposition among graphene sheets, and enable highly reversible lithium stripping with minimal residue caused by the benign structure of deposited lithium. Meanwhile, the LiF and Li_3N-rich inorganic SEI formed *in situ* on LAG can protect the as-deposited lithium, and even facilitate lithium plating/stripping cycling, while LA103Z can continuously compensate for lithium loss.

3. Conclusions

Free-standing porous graphene films decorated with lithiophilic particles of AlN@Li_3N, MgF_2, and Li_2CO_3, and the LA103Z foil are designed and fabricated as host electrodes for AL-LMBs. The alkalization, AlN and MgF_2 loading, and fast thermal reduction afford the as-prepared films with highly reversible and stable lithium plating/stripping performance at a current density of 5 mA cm^{-2} and a capacity of 5 mA h cm^{-2}.

Specifically, the thin LA103Z foil can compensate for lithium loss during long-term lithium plating/stripping. The pre-loaded AlN@Li_3N and MgF_2 can enhance the formation of a LiF- and Li_3N-rich inorganic SEI, which suppresses electrolyte-related side-reactions, facilitates Li^+ transport, promotes Li^+ desolvation, reduces interfacial resistance, and stabilizes lithium plating/stripping. With its unique composition and morphology, the AL-LMB assembled with a LAG film adhered to LA103Z foil as the host electrode and NCM811 as the cathode, LAG/LA103Z||NCM811, can achieve a capacity retention of ~60% after 120 cycles at 3.86 mA h cm^{-2} and 1.93 mA cm^{-2} in a carbonate-based electrolyte. This work proposes the practical application of free-standing graphene films as host electrodes in high-performance AL-LMBs.

4. Experimental section

4.1. Material preparation

GO powders were purchased from Xi'an Times Graphene New Energy Technology Co., Ltd (Shaanxi, China). The GO was suspended in deionized water under ultrasonication for 30 min and then stirred for 24 h to get the GO precursor solution of 3 mg mL^{-1}. Prior to decoration with inorganic particles, the GO was alkalized by adding LiOH in the GO solution until the LiOH concentration reached 0.1 M (pH = 13). The AlN and MgF_2 particles were decorated on the GO sheets by mixing the corresponding particles with the alkalized GO solution, and then vacuum filtered using cellulose membranes with a diameter of 50 and an aperture of 0.22 μm. The mass ratios of AlN and MgF_2 to GO were kept below 1 : 10 to reduce their effects on the thin film formation. The as-obtained films were washed with ethyl alcohol (95%), dried at 50 °C for 20 min, and then further annealed at 500 °C for 30 min with the heating rates of ~50 °C s^{-1}. During the procedure, the GO was reduced, and the thin films were named AG and LAG, with and without inorganic particles, respectively. All thermal reduction processes were conducted in an air atmosphere, using a tube furnace (Hefei Kejing Materials Technology Co., Ltd, Anhui, China).

Mg–Li alloy foil with a thickness of 50 μm, known as LA103Z, was purchased from Suzhou Xinghai Electronic Business Co., Ltd (Jiangsu, China). The LA103Z foil was first pickled in chromic acid solution (90 g L^{-1} CrO_3, and 25 g L^{-1} $LiNO_3$ aqueous solution) for ~3 min, and then thoroughly cleaned under ultrasonication in ultrapure water and ethyl alcohol (95%), until a white metallic surface was observed. The LAG film and pickled LA103Z foil was rolled together at 50 °C on an electric roller (Hefei Kejing Materials Technology Co., Ltd, Anhui, China) to get the LAG/LA103Z bilayer film.

4.2. Characterization

X-ray microscopy (XRM) images were obtained on an Xradia 520 Versa X-ray microscope (Carl Zeiss, Germany), operated at an accelerating voltage of 80 kV, and a voxel resolution of 0.5052 μm. The 3D-reconstruction of the XRM images was processed using Dragonfly Pro software (Comet Technologies Canada Inc.) based on density. Scanning electron microscopy (SEM) images and energy-dispersive X-ray spectroscopy (EDS) data were acquired using a NOVA NanoSEM 230 field emission scanning electron microscope (Thermo Fisher Scientific, U. S. A). The top-view SEM images were recorded in back scattered electrons mode, while secondary electrons were used for the cross-sectional (side-view) imaging.

Transmission electron microscopy (TEM) and high-resolution TEM (HRTEM) images were obtained on a Talos F200X field emission transmission electron microscope (Thermo Fisher Scientific, U. S. A). For TEM imaging, the film was ground and dispersed into dimethyl carbonate (DMC), and then loaded onto the TEM grid. HRTEM was performed at an accelerating voltage of 200 kV. X-ray diffraction (XRD) patterns were obtained on an Aeris metals edition X-ray diffractometer (Malvern Panalytical, China) with Cu K_α irradiation (λ = 0.154 nm), at a scanning rate of 2° min^{-1}. X-ray photoelectron spectroscopy (XPS) measurements were conducted on an EscaLab Xi+ X-ray photoelectron spectrometer (Thermo Fisher Scientific, U. S. A). All XPS spectra were calibrated using the 284.8 eV C 1s peak of C–C/C–H as the reference. Thermogravimetric analysis (TGA) was performed from room temperature to 700 °C at a heating rate of 10 °C min^{-1} in an air atmosphere on a TGA8000 instrument (PerkinElmer, U. S. A). Since Li_2CO_3 is introduced through the alkalization process and the component differences between the AG and LAG films are AlN@Li_3N and MgF_2, the mass ratio of Li_2CO_3 is calculated by the difference between the AG and GO ash remnants, while the mass ratios of AlN@Li_3N and MgF_2 are calculated by the difference between the LAG and AG ash remnants. Raman spectra were obtained using an inVia Qontor (Renishaw, U. K.) at an excitation laser wavelength of 532 nm. The Attenuated Total Reflection Infrared (ATR-IR) spectra were acquired on an EQUINOX 55 FTIR spectrometer (Bruker, Germany).

Zeta potentials were measured in water, 0.1 M LiOH aqueous solution, and DMC, using a Zetasizer Nano ZSE instrument (Malvern Panalytical, China). The samples for zeta-potential measurements were prepared by suspending the solid particles in the liquid phase at a concentration 0.5 mg mL^{-1}. The particle size distributions of AlN and MgF_2 were evaluated on a Mastersizer 3000 instrument (Malvern Panalytical, China). Nitrogen adsorption analysis was conducted at 77.35 K using an ASAP2460 aperture analyzer (Micromeritics, U. S. A). To avoid false peaks at ~3.8 nm in desorption curves, BJH analyses were based only on adsorption curves. Tensile stress–strain tests were performed on a Discovery DMA800 instrument (TA Instruments-Waters LLC, U. S. A). Contact-angles were measured with water and DMC (5 μL) on a DSA100 instrument (Kruss, Germany). Inductively coupled plasma optical emission spectroscopy (ICP-OES) measurements were conducted on an Avio 500 spectrometer (PerkinElmer, Singapore). For the XPS, SEM, TEM, and ICP-OES measurements on the electrodes after lithium plating and stripping cycles, the bilayer thin films were thoroughly rinsed with DMC to remove residual electrolyte. The preparation and transfer of the cycled electrodes were conducted in an argon-filled glovebox to avoid the effects of oxygen and water vapor in air.

4.3. Electrochemical measurements

All electrochemical measurements were carried out on CR2025 coin cells assembled in a glove box filled with argon. For half-cell cycling assembly, the as-prepared thin bilayer films were cut into disks with a diameter of 12 mm as working electrodes; commercial Li foil (16 mm in diameter, and ~100 μm in thickness) was used as the counter electrodes, and 1 M $LiPF_6$ in ethylene carbonate (EC)/diethyl carbonate (DEC)/dimethyl carbonate (DMC) (1/1/1, in vol) with 10 vol% fluoroethylene carbonate (FEC) was used as the electrolyte. To get a proper average CE, the initial 5 cycles were excluded to better assess lithium plating and stripping reversibility.[39,52] The constant current lithium plating (discharging) and stripping (charging) mode was chosen for coin half-cell cycling.

The full cells were constructed with Cu, LAG, and LAG/LA103Z as host electrodes, and NCM811 as the cathode. Before full-cell assembly, LAG, and LAG/LA103Z were pre-cycled in half-cells between 0.01 and 1 V, to eliminate initial irreversible lithium consumption, while maintaining them in the delithiation state without excess lithium.[52,53] The loading mass of NCM811 on the cathode was 20 mg cm^{-2}, with an areal capacity of 3.86 mA h cm^{-2}. The electrolyte used in the full-cell is the same as that used in the half-cell. A Celgard 2400 film was used as the separator. All full-cells were charged and discharged at 0.05C (0.193 mA cm^{-2}) for the initial 2 cycles, then charged at 0.5C (1.93 mA cm^{-2}) to 4.2 V, with constant-voltage charging at 4.2 V until the current decreased to 0.05C, and then discharged at 0.5C to 2.5 V. The electrochemical impedance spectroscopy (EIS) data were collected by applying a perturbation voltage of 5 mV *versus* the open-circuit potential in a frequency range from 10^6 to 0.01 Hz. All galvanostatic charge–discharge (GCD) curves were measured on a LAND-CT2001A electrochemical workstation (Wuhan LAND, China), while CV and EIS data were acquired on an AUTOLAB electrochemical workstation (Metrohm, Switzerland).

Data availability

The data supporting this article have been included as part of the ESI.†

Author contributions

Mingliang Bai: conceptualization, data curation, formal analysis, investigation, methodology, writing – original draft. Min Zhong: funding acquisition, methodology, resources, supervision, writing – review & editing. Wenzhuo Shen: funding acquisition, resources. Jiali Zhang: funding acquisition, resources. Shouwu Guo: funding acquisition, methodology, resources, supervision, writing – review & editing.

Conflicts of interest

There are no conflicts to declare.

Acknowledgements

The authors wish to express their appreciation to the Instrument Analysis Centre of SJTU. We are grateful for the discussion on the XPS data with Ms Xue Ding and XRM data with Ms Yanhua Zhu at the Instrumental Analysis Centre of Shanghai Jiao Tong University.

References

1 A. Masias, J. Marcicki and W. A. Paxton, *ACS Energy Lett.*, 2021, **6**, 621–630.
2 H. Li, *Joule*, 2019, **3**, 911–914.
3 P. Albertus, V. Anandan, C. Ban, N. Balsara, I. Belharouak, J. Buettner-Garrett, Z. Chen, C. Daniel, M. Doeff, N. J. Dudney, B. Dunn, S. J. Harris, S. Herle, E. Herbert, S. Kalnaus, J. A. Libera, D. Lu, S. Martin, B. D. McCloskey, M. T. McDowell, Y. S. Meng, J. Nanda, J. Sakamoto, E. C. Self, S. Tepavcevic, E. Wachsman, C. Wang, A. S. Westover, J. Xiao and T. Yersak, *ACS Energy Lett.*, 2021, **6**, 1399–1404.
4 W. Xu, J. Wang, F. Ding, X. Chen, E. Nasybulin, Y. Zhang and J.-G. Zhang, *Energy Environ. Sci.*, 2014, **7**, 513–537.
5 M. Yeddala, L. Rynearson and B. L. Lucht, *ACS Energy Lett.*, 2023, **8**, 4782–4793.
6 C.-J. Huang, H.-C. Tao, P.-J. Chao, C.-Y. Li, B. T. Hotasi, H.-Y. Liu, M.-H. Lin, S.-H. Wu, W.-N. Su and B. J. Hwang, *ACS Nano*, 2023, **17**, 13241–13255.
7 A. J. Sanchez and N. P. Dasgupta, *J. Am. Chem. Soc.*, 2024, **146**, 4282–4300.
8 T. T. K. Ingber, M. M. Bela, F. Püttmann, J. F. Dohmann, P. Bieker, M. Börner, M. Winter and M. C. Stan, *J. Mater. Chem. A*, 2023, **11**, 17828–17840.
9 C. Liu, B. Wu, Y. Zhang, T. Liu, J. Cui, L. Huang, G. Tan, L. Zhang, Y. Su and F. Wu, *J. Mater. Chem. A*, 2023, **11**, 25455–25464.
10 Z. Tong, B. Bazri, S.-F. Hu and R.-S. Liu, *J. Mater. Chem. A*, 2021, **9**, 7396–7406.
11 P. Liu, S. Shen, Z. Qiu, T. Yang, Y. Liu, H. Su, Y. Zhang, J. Li, F. Cao, Y. Zhong, X. Liang, M. Chen, X. He, Y. Xia, C. Wang, W. Wan, J. Tu, W. Zhang and X. Xia, *Adv. Mater.*, 2024, **36**, 2312812.
12 R. M. Kasse, N. R. Geise, J. S. Ko, J. Nelson Weker, H.-G. Steinrück and M. F. Toney, *J. Mater. Chem. A*, 2020, **8**, 16960–16972.
13 P. Ma, R. Kumar, M. C. Vu, K.-H. Wang, P. Mirmira and C. V. Amanchukwu, *J. Mater. Chem. A*, 2024, **12**, 2479–2490.
14 A. J. Louli, A. Eldesoky, R. Weber, M. Genovese, M. Coon, J. deGooyer, Z. Deng, R. T. White, J. Lee, T. Rodgers, R. Petibon, S. Hy, S. J. H. Cheng and J. R. Dahn, *Nat. Energy*, 2020, **5**, 693–702.
15 D. Wang, J. Qiu, N. Inui, R. Hagiwara, J. Hwang and K. Matsumoto, *ACS Energy Lett.*, 2023, **8**, 5248–5252.
16 K. B. Hatzell, *ACS Energy Lett.*, 2023, **8**, 4775–4776.
17 J.-J. Woo, V. A. Maroni, G. Liu, J. T. Vaughey, D. J. Gosztola, K. Amine and Z. Zhang, *J. Electrochem. Soc.*, 2014, **161**, A827.

18 T. Lyu, F. Luo, D. Wang, L. Bu, L. Tao and Z. Zheng, *Adv. Energy Mater.*, 2022, **12**, 2201493.
19 Q. Zhang, L. Xu, X. Yue, J. Liu, X. Wang, X. He, Z. Shi, S. Niu, W. Gao, C. Cheng and Z. Liang, *Adv. Energy Mater.*, 2023, **13**, 2302620.
20 D. W. Kang, S. S. Park, H. J. Choi, J.-H. Park, J. H. Lee, S.-M. Lee, J.-H. Choi, J. Moon and B. G. Kim, *ACS Nano*, 2022, **16**, 11892–11901.
21 S. Zhang, S. Xiao, D. Li, J. Liao, F. Ji, H. Liu and L. Ci, *Energy Storage Mater.*, 2022, **48**, 172–190.
22 T. Yang, L. Li, F. Wu and R. Chen, *Adv. Funct. Mater.*, 2020, **30**, 2002013.
23 C. Gao, J. Kang, Y. Zhang, C. He, C. Shi, B. Chen, L. Ma, E. Liu, J. Sha, F. Zhou and N. Zhao, *Chem. Commun.*, 2024, **60**, 9130–9148.
24 T. Li, Z. Qiu, T. Zhang, H. Liao, C. Li, B. Ye, Q. Xiong, Y. Zhang and X. Xia, *Electrochim. Acta*, 2024, **494**, 144427.
25 K. Lin, X. Qin, M. Liu, X. Xu, G. Liang, J. Wu, F. Kang, G. Chen and B. Li, *Adv. Funct. Mater.*, 2019, **29**, 1903229.
26 H. Chen, Y. Yang, D. T. Boyle, Y. K. Jeong, R. Xu, L. S. de Vasconcelos, Z. Huang, H. Wang, H. Wang, W. Huang, H. Li, J. Wang, H. Gu, R. Matsumoto, K. Motohashi, Y. Nakayama, K. Zhao and Y. Cui, *Nat. Energy*, 2021, **6**, 790–798.
27 H. Yao, F. Niu, C. Ma, X. You, D. Ning, J. Qian, M. Wang, Q. Duan, C. Yang, Q. Wu, J. Wang, J. Zhang, Z. Lu, C. Yang and W. Wu, *Adv. Funct. Mater.*, 2024, **34**, 2310711.
28 K. Kim and Y. Lee, *Nucl. Eng. Technol.*, 2021, **53**, 2341–2347.
29 D. X. Wu, J. He, J. D. Liu, M. G. Wu, S. A. Qi, H. P. Wang, J. D. Huang, F. Li, D. L. Tang and J. M. Ma, *Adv. Energy Mater.*, 2022, **12**, 2200337.
30 X. Chen, W. Li, D. Luo, M. Huang, X. Wu, Y. Huang, S. H. Lee, X. Chen and R. S. Ruoff, *ACS Nano*, 2017, **11**, 665–674.
31 X. Chen, D. Meng, B. Wang, B.-W. Li, W. Li, C. W. Bielawski and R. S. Ruoff, *Carbon*, 2016, **101**, 71–76.
32 M. H. Brooker and J. Wang, *Spectrochim. Acta, Part A*, 1992, **48**, 999–1008.
33 H. Wan, J. Xu and C. Wang, *Nat. Rev. Chem*, 2024, **8**, 30–44.
34 M. S. Kim, Z. Zhang, J. Wang, S. T. Oyakhire, S. C. Kim, Z. Yu, Y. Chen, D. T. Boyle, Y. Ye, Z. Huang, W. Zhang, R. Xu, P. Sayavong, S. F. Bent, J. Qin, Z. Bao and Y. Cui, *ACS Nano*, 2023, **17**, 3168–3180.
35 K. Yan, Z. Lu, H.-W. Lee, F. Xiong, P.-C. Hsu, Y. Li, J. Zhao, S. Chu and Y. Cui, *Nat. Energy*, 2016, **1**, 16010.
36 X.-R. Chen, B.-C. Zhao, C. Yan and Q. Zhang, *Adv. Mater.*, 2021, **33**, 2004128.
37 H.-S. Lim, D. T. Nguyen, J. A. Lochala, X. Cao and J.-G. Zhang, *ACS Energy Lett.*, 2024, **9**, 126–135.
38 P. Peljo and H. H. Girault, *Energy Environ. Sci.*, 2018, **11**, 2306–2309.
39 S. Cho, D. Y. Kim, J.-I. Lee, J. Kang, H. Lee, G. Kim, D.-H. Seo and S. Park, *Adv. Funct. Mater.*, 2022, **32**, 2208629.
40 W. Chen, R. V. Salvatierra, M. Ren, J. Chen, M. G. Stanford and J. M. Tour, *Adv. Mater.*, 2020, **32**, 2002850.
41 S. C. Kim, J. Wang, R. Xu, P. Zhang, Y. Chen, Z. Huang, Y. Yang, Z. Yu, S. T. Oyakhire, W. Zhang, L. C. Greenburg, M. S. Kim, D. T. Boyle, P. Sayavong, Y. Ye, J. Qin, Z. Bao and Y. Cui, *Nat. Energy*, 2023, **8**, 814–826.
42 X. Liao, X. Wang, C. Yan, B. Zhang, Y. Ni, H. Yuan, Y. Pan, J. a. Pan and J. Huang, *Adv. Funct. Mater.*, 2024, 2310925, DOI: **10.1002/adfm.202310925**.
43 X.-Q. Zhang, X.-B. Cheng, X. Chen, C. Yan and Q. Zhang, *Adv. Funct. Mater.*, 2017, **27**, 1605989.
44 Y. Zhang, F. Li, Y. Cao, M. Yang, X. Han, Y. Ji, K. Chen, L. Liang, J. Sun and G. Hou, *Adv. Funct. Mater.*, 2024, **34**, 2315527.
45 Z. Jiang, T. Yang, C. Li, J. Zou, H. Yang, Q. Zhang and Y. Li, *Adv. Funct. Mater.*, 2023, **33**, 2306868.
46 S. Zhang, R. Li, N. Hu, T. Deng, S. Weng, Z. Wu, D. Lu, H. Zhang, J. Zhang, X. Wang, L. Chen, L. Fan and X. Fan, *Nat. Commun.*, 2022, **13**, 5431.
47 J. Tan, J. Matz, P. Dong, J. Shen and M. Ye, *Adv. Energy Mater.*, 2021, **11**, 2100046.
48 Y.-H. Tan, Z. Liu, J.-H. Zheng, Z.-J. Ju, X.-Y. He, W. Hao, Y.-C. Wu, W.-S. Xu, H.-J. Zhang, G.-Q. Li, L.-S. Zhou, F. Zhou, X. Tao, H.-B. Yao and Z. Liang, *Adv. Mater.*, 2024, **36**, 2404815.
49 C. Ma, Q. Qiao, K. Yue, J. Yue, X. Cai, J. Zheng, L. Kang, Y. Wang, J. Nai, J. Luo, H. Yuan, S. Zou, X. Tao and Y. Liu, *Adv. Funct. Mater.*, 2024, 2406479, DOI: **10.1002/adfm.202406479**.
50 E. W. C. Spotte-Smith, T. B. Petrocelli, H. D. Patel, S. M. Blau and K. A. Persson, *ACS Energy Lett.*, 2023, **8**, 347–355.
51 G.-X. Li, H. Jiang, R. Kou, D. Wang, A. Nguyen, M. Liao, P. Shi, A. Silver and D. Wang, *ACS Energy Lett.*, 2022, **7**, 2282–2288.
52 C. Cui, C. Yang, N. Eidson, J. Chen, F. Han, L. Chen, C. Luo, P.-F. Wang, X. Fan and C. Wang, *Adv. Mater.*, 2020, **32**, 1906427.
53 C. Wang, M. Liu, M. Thijs, F. G. B. Ooms, S. Ganapathy and M. Wagemaker, *Nat. Commun.*, 2021, **12**, 6536.